

High-Energy Reaction Dynamics of N_3

JingChun Wang,^{†,§} Juan Carlos San Vicente Veliz,^{†,‡,§} and Markus Meuwly^{*,†,¶}

[†]*Department of Chemistry, University of Basel, Klingelbergstrasse 80, CH-4056 Basel, Switzerland*

[‡]*Present Address: Department of Chemistry, Temple University, 1801 N Broad St, Philadelphia, PA 19122, United States*

[¶]*Department of Chemistry, Brown University, RI 02912, USA*

[§]*These authors contributed equally*

E-mail: m.meuwly@unibas.ch

Abstract

The atom-exchange and atomization dissociation dynamics for the $N(^4S) + N_2(^1\Sigma_g^+)$ reaction is studied using a reproducing kernel Hilbert space (RKHS)-based, global potential energy surface (PES) at the MRCI-F12/aug-cc-pVTZ-F12 level of theory. For the atom exchange reaction ($N_A N_B + N_C \rightarrow N_A N_C + N_B$), computed thermal rates and their temperature dependence from quasi-classical trajectory (QCT) simulations agree to within error bars with the available experiments. Companion QCT simulations using a recently published CASPT2-based PES confirm these findings. For the atomization reaction, leading to three $N(^4S)$ atoms, the computed rates from the RKHS-PES overestimate the experimentally reported rates by one order of magnitude whereas those from the PIP-PES agree favourably, and the T -dependence of both computations is consistent with experiment. These differences can be traced back to the different methods and basis sets used. The lifetime of the metastable N_3 molecule is estimated to be ~ 200 fs depending on the initial state of the reactants. Finally, neural network-based

exhaustive state-to-distribution models are presented using both PESs for the atom exchange reaction. These models will be instrumental for a broader exploration of the reaction dynamics of air.

April 30, 2024

Introduction

Among the pivotal reactions for high-energy gas flows are the $\text{N}(^4\text{S}) + \text{N}_2(^1\Sigma_g^+)$ atom exchange ($\text{N}_\text{A}\text{N}_\text{B} + \text{N}_\text{C} \rightarrow \text{N}_\text{A}\text{N}_\text{C} + \text{N}_\text{B}$) and dissociation reactions to three $\text{N}(^4\text{S})$ atoms.^{1,2} The atom exchange reaction $\text{N}_\text{A}(^4\text{S}) + \text{N}_\text{B}\text{N}_\text{C}(^1\Sigma_g^+) \rightarrow \text{N}_\text{B}(^4\text{S}) + \text{N}_\text{A}\text{N}_\text{C}(^1\Sigma_g^+)$ is particularly important for the energy content and redistribution in reactive high-energy flows as they occur in atmospheric re-entry (hypersonics) and combustion. Molecular nitrogen $\text{N}_2(^1\Sigma_g^+)$ is also the main constituent of Earth’s atmosphere and abundant in the atmospheres of Titan, Triton, and Pluto.^{3,4} Therefore, the chemistry involving N_2 is particularly relevant for characterizing and understanding the chemical composition and evolution of such atmospheres. In interstellar environments, electron irradiation of N_2 ices lead to N_3 as a product, among others.⁵

The intermolecular interactions and reactive dynamics of N_3 have been studied using experiments and calculations. One of the earlier computational works considered linear, bent and cyclic- N_3 in its doublet and quartet states from multireference calculations with particular focus on its unimolecular dissociation.⁶ Specifically, it was reported that bent N_3 in its quartet state is metastable with respect to the $\text{N}(^4\text{S}) + \text{N}_2(^1\Sigma_g^+)$ ground state products which is also of interest in the present work. Several potential energy surfaces (PESs) for the quartet state reaction have been published. One of the earlier attempts was an empirical London-Eyring-Polanyi-Sato (LEPS) PES.⁷ A later PES used CCSD(T) and internally contracted multireference configuration interaction calculations with different basis sets (cc-

pVQZ, aug-cc-pVTZ) which were fitted to a many-body expansion.⁸ This was followed by CCSD(T)/aug-cc-pVTZ-based PESs fitted to different functional forms⁹ and a PES for N_3 derived¹⁰ from a PES for N_4 .¹¹ Most recently, a permutationally invariant polynomial (PIP) representation for the $N(^4S) + N_2(^1\Sigma_g^+)$ PES based on CASPT2/maug-cc-pVQZ reference energies was reported.¹²

Dynamics studies using some of these PESs considered the computation of thermal rates for the atom exchange^{8,13,14} and dissociation reactions.^{10,15,16} Comparisons with experiments were possible for a few high-temperature measurements for both reactions.^{17,18} For the dissociation reaction experiments were carried out between 8000 K and 15000 K,¹⁸ whereas for the atom exchange reaction experiments are available at two temperatures (3400 K and at ~ 1300 K).^{17,19}

The state-to-state cross sections for atom+diatom reactions are an essential ingredient for microscopic modeling of reactive gas flow.² Using high-level electronic structure calculations for full-dimensional, reactive and global potential energy surfaces together with their representation and dynamics simulations provides - in principle - the necessary information for their computation. However, characterizing the state-to-state reaction cross sections and rates even for triatomics is a daunting task. Machine-learning-based methods can provide computationally effective means to exhaustively sample them without the need for explicit calculation based on, for example, quasi-classical trajectory (QCT) simulations.²⁰⁻²²

The present work determines a new full-dimensional reactive PES for the $N(^4S) + N_2(^1\Sigma_g^+)$ collision system at the multi reference configuration interaction (MRCI) level of theory, complementing the existing PESs for the [NNO], [OON], and [OOC] reaction systems using the same methods.²³⁻²⁶ Given this PES, thermal rates for atom-exchange and dissociation reactions are determined together with state-to-distribution (STD) models for the atom ex-

change reaction. These are the basis for a comprehensive treatment of air burning at high temperatures. The results are compared with experiments, where available, and with QCT simulations using a recent PIP-represented CASPT2/maug-cc-pVQZ PES which has, to the best of our knowledge, not yet been used for computing rates for the atom exchange reaction. For direct comparison, STD models were also trained from QCT simulations using the CASPT2 PES.

The remainder of this paper is organized as follows. First the computational methods are introduced. This is followed by a characterization of the new PES and its validation for the $\text{N}(^4\text{S}) + \text{N}_2(^1\Sigma_g^+)$ atom-exchange and dissociation reactions. Next, state-to-distribution models are generated and discussed and finally, conclusions are drawn.

Methods

Potential Energy Surface Construction

The $\text{N}_2(^1\Sigma_g^+) + \text{N}(^4\text{S})$ collision correlates with the ($^4\text{A}''$) electronic state. For the reference energies, electronic structure calculations were carried out using the aug-cc-pVTZ-F12 (AVTZ-F12) basis set at the MRCI-F12 level of theory using the MOLPRO suite of codes.²⁷ For the MRCI-F12 calculations, multistate CASSCF(15,12) calculations - consistent with previous work^{6,28} - were carried out to correctly characterize the wave function which was then used as the starting point for the MRCI-F12 calculations. Preference of explicitly correlated MRCI-F12 over conventional MRCI calculations was given because a larger number of correctly converged energies across the grid were obtained (see below) due to the improved basis set convergence of the MRCI-F12 method.²⁹ A total of 8 states, two per spin state (doublet and quartet), and symmetry group were included in the state-averaged calculations.

As is well-known for such calculations, there are nuclear geometries for which either the CASSCF or the MRCI-F12 calculations do not converge to the correct electronic states or do not converge at all. Such energies were removed and the grid was reconstructed and completed (“cleaned”) using a 2D RKHS $V(R, r)$ to evaluate the missing points. The grid for the reference calculations was $R = [1.4, 1.6, 1.8 \cdots 5.0, 5.25, 5.5, 5.8, 6.1, 6.5, 7.0, 8.0, 9.5, 11.0, 13.0]$ a_0 , $r = [1.5, 1.6 \cdots 2.0, 2.05, 2.1, 2.15, 2.25, 2.35, 2.5 \cdots 3.1, 3.3 \cdots 4.1]$ a_0 , and $\theta = [172.128, 161.929, 151.671, 141.399, 131.123, 120.843, 110.563, 100.281, 90.000]^\circ$ with the other half of the angles defined by symmetry. Using this cleaned grid the 3-dimensional RKHS representation was constructed. The permutationally invariant reactive PES $V(\mathbf{r}) = \sum_{i=1}^3 \omega_i(r_i)V_i(\mathbf{r})$ was constructed by mixing the three possible channels $N_A N_B + N_C$, $N_A N_C + N_B$, and $N_B N_C + N_A$ using an exponential switching function

$$w_i(r) = \frac{e^{-(r_i/\rho_j)^2}}{\sum_{j=1}^3 e^{-(r_j/\rho_j)^2}} \quad (1)$$

for a given structure \mathbf{r} of N_3 . The fitted mixing parameters were $\rho_1 = \rho_2 = \rho_3 = 1.0 a_0$. The RKHS-PES was constructed from 5481 reference energies, compared with 7174 energies for the PIP-PES determined at the CASPT2/maug-cc-pVQZ (mAVQZ) level of theory. The CASPT2 calculations use a smaller CAS(9,9) active space, including the two lowest states in the CASSCF calculations with weights of 0.9 and 0.1, respectively, and an imaginary shift of 0.1 a.u. in the CASPT2 calculations to reproduce the experimentally reported N_2 dissociation energy.¹²

QCT Simulations

For thermal rates (atom insertion and full dissociation) 10^7 independent QCT simulations were carried out for a given temperature. Semiclassical initial conditions were sampled from Boltzmann distributions for vibrational quantum number v , rotational quantum number j ,

total angular momentum J , impact parameter b , and collision energy E_{trans} . The thermal rates at given temperature T were then obtained from

$$k(T) = g_e(T) \sqrt{\frac{8k_B T}{\pi\mu}} \pi b_{\text{max}}^2 \frac{N_r}{N_{\text{tot}}}, \quad (2)$$

where $g_e(T)$ is the electronic degeneracy factor, μ is the reduced mass of the collision system, k_B is the Boltzmann constant, and N_r is the number of reactive trajectories (either N-atom exchange or N₃-atomization). For the exchange reaction, $g_e(T) = 1$ whereas for the full dissociation reaction, $g_e(T) = q_{N(4S)}^3 / (q_{N(4S)} q_{N_2}) = 16$. However, to avoid inflating rates based on state-counts alone, $g_e = 1$ was used for the atomization reaction as well. The sampling methodology was discussed in detail in Ref.²⁶ Statistical errors were quantified through bootstrapping. For this, 10⁶ samples with 10 random shuffles of the data (100 times of resamples in total) were used to yield the expectation values of thermal rates along with the standard deviations.

For the STD models, QCT simulations were carried out on a grid of initial conditions. These included $v = [0, 2 \dots 8, 10, 12, 15 \dots 30, 34, 38]$, $j = [0, 15, 30 \dots 225]$, and $E_{\text{col}} = [0.5, 1.0, 1.5 \dots 5.0, 6.0, 7.0, 8.0]$ eV. State-specific QCT simulations were carried out for a total of 80000 trajectories per initial condition and stratified sampling was used for the impact parameter $b = [0, b_{\text{max}} = 12.0 a_0]$. The maximum allowed propagation time was 75 ps and runs were terminated when the sum of all atom separations was larger than 12 a_0 .

STD training and evaluation

One approach to creating a model that spans all possible probabilities for the outcome of a collision between an atom and a diatom is to use a neural network (NN) representation.²¹ Such an NN consists of seven residual layers with two hidden layers per residual layer, and

uses 11 input and 161 output nodes corresponding to the 11 features representing the initial reactant state and the 161 amplitudes characterizing the product state distributions. For training, the NN inputs were standardized which ensures that the distributions of the transformed inputs x'_i over the entire training data are each characterized by $(\bar{x}'_i = 0, \sigma'_i = 1)$. The NN outputs were normalized which ensures that the distributions of the transformed outputs x'_i over the entire training data being characterized by $(\bar{x}'_i = \bar{x}_i, \sigma'_i = 1)$. Standardization of the data generally yields a faster convergence.³⁰ The loss function was the root-mean-squared deviation between reference QCT final state distributions $[P(E'_{\text{trans}}), P(v'), P(j')]$ and model predictions. As the NN outputs are probabilities, being non-negative even after normalization, a softplus function is used as the activation function of the output layer.

For training, the weights and biases of the NN were initialized according to the Glorot scheme³¹ and optimized using Adam³² with an exponentially decaying learning rate. The NN was trained using TensorFlow³³ and the weights and biases resulting in the smallest loss as evaluated on the validation set were subsequently used for prediction. Overall, final state distributions from 3081 initial conditions on a grid defined by $(0.5 \leq E'_c \leq 5.0)$ eV with $\Delta E'_c = 0.5$ eV and $(5.0 \leq E'_c \leq 8.0)$ eV with $\Delta E'_c = 1.0$ eV, $v' = [0, 2, 4, 6, 8, 10, 12, 15, 18, 21, 24, 27, 30, 34, 38]$, and $0 \leq j' \leq 272$ with step size $\Delta j' = 15$ were generated.

The results of the QCT simulations starting from 3081 initial conditions were collected for generating the dataset. Simulations from 1130 initial conditions yield insufficiently low reaction probabilities $\sum_{v'=0}^{v'_{\text{max}}} P(v') < 0.02$ for convergence and are thus excluded from the training set. Initial conditions for these low-probability final states are characterized by low and extremely high $[E_{\text{trans}}, v, j]$ values. This is because for low initial values the atom exchange reaction is improbable to occur whereas for the largest translational and/or internal energies, atomization to $3\text{N}(^4\text{S})$ is the dominant final state.

The final dataset (final state distributions from 2360 initial conditions) will be referred to “on-grid” in the following. A 80:10:10 split of the dataset was randomly drawn for training, validation and testing.²¹ The “on-grid” dataset is to be distinguished from “off-grid” final state distributions that originate from initial conditions which differ in any of the $[E_{\text{trans}}, v, j]$ quantum numbers used for training. For additional technical details, see Ref.²¹

Results

Topography of the $\text{N}_2(^1\Sigma_g^+) + \text{N}(^4\text{S})$ PES

The performance of the RKHS-representation for on- and off-grid reference MRCI-F12 energies is reported in Figure S1. For the single-channel PES the RMSD/MAD for the training (on-grid) points are 0.03/0.01 kcal/mol across an energy range of ~ 10 eV (~ 230 kcal/mol), see Figure S1A. The permutationally invariant, mixed PES features RMSD/MAD of 0.45/0.08 kcal/mol with a few outliers at high energies (Figure S1B) whereas evaluating this PES on off-grid energies leads to RMSD/MAD of 1.50/0.73 kcal/mol, see Figure S1C. Again, small outliers are found at the highest energies. Restricting the dataset to energies between -7 and 0 eV in Figure S1C yields RMSD/MAE of 1.25/0.69 kcal/mol, respectively. This compares with root mean squared errors ranging from 1.5 to 3.7 kcal/mol for on-grid points covering a comparable energy range for the PIP-PES.¹²

Two-dimensional representations $V(R, \theta; r = r_{\text{eq}})$ of the RKHS-PES (solid lines) and PIP-PES (dashed lines) are reported in Figure 1. The topography of the two PESs is comparable in their overall shapes, but there are notable differences in details. Both PESs are symmetric with respect to $\theta = 90^\circ$, as expected. The computed minimum energy structures on the RKHS-PES are clearly identified at $R = 3.25 a_0$, $\theta = 43.5^\circ$ and symmetrically at $R = 3.25 a_0$, $\theta = 136.5^\circ$, which agree closely with positions of the minima for the PIP-PES,

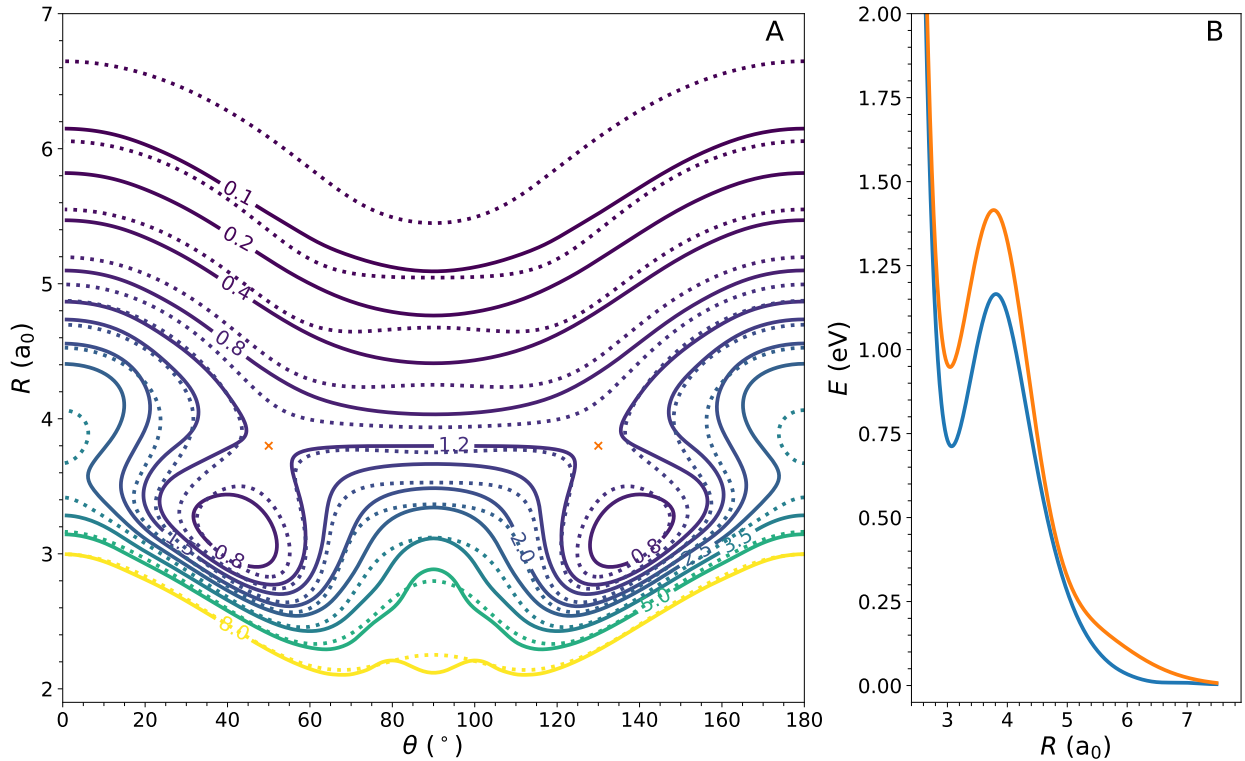


Figure 1: Panel A: 2D contour representations of $V(R, \theta)$ at the N_2 minimum energy structure for the RKHS representation (solid lines, $r_{\text{NN}} = 2.39 \text{ a}_0$), and the PIP fit of the CASPT2 reference data¹² (dashed lines, $r_{\text{NN}} = 2.40 \text{ a}_0$). Isocontours are labelled by energy difference in eV relative to $E(\text{N}_2(1^1\Sigma_g^+; r = r_e) + E(\text{N}))$, of the specific cut of the PES. Panel B: 1D cuts $V(R)$ along $\theta = 130^\circ$ in panel A for the RKHS-PES (blue) and the PIP-PES (orange).

see Figure 1 and Table 1. The calculated transition state geometries (orange crosses) are at $R = 3.96 a_0$, $\theta = 52.0^\circ$ and symmetrically at $R = 3.96 a_0$, $\theta = 128.0^\circ$, which are also close to those on the PIP-PES. The geometries and energies for the critical points of both PESs are summarized in Table 1 and compared with earlier calculations as well. Note that the table reports valence angles $\angle N_A N_B N_C$ instead of Jacobi angles θ .

In the long-range part of the intermolecular interactions the PIP-PES extends further along R than the RKHS-PES, see the 0.1 eV isocontours in Figure 1. The isocontours at 0.2, 0.4 and 0.8 eV for the RKHS-PES point to a conventional $P_2(\cos(\theta))$ -dependence whereas for the PIP-PES the region between $\theta \in [60, 120]^\circ$ is predominantly flat with a faint undulation superimposed. This is also observed for isocontours at longer R -range and points towards a somewhat different angular anisotropy of the two PESs. Additional 2D contour plots $V(R, \theta)$ and $V(r_{AB}, r_{BC})$ in Figures S2 and S3 underline the similarities and differences between the RKHS-PES and PIP-PES.

The minimum energy and transition state structures and energies for the present RKHS-PES were determined using the nudged elastic band (NEB) method.³⁴ For the local minimum an isosceles triangle with bond lengths of $2.39 a_0$ and a valence angle of 118° was found, see Table 1. The minimum energy structure is 43.7 kcal/mol above the dissociation to $N_2(^1\Sigma_g^+) + N(^4S)$. Using the PIP-PES the bond length is $2.40 a_0$ and the valence angle reduces to 115.5° . This compares favourably with the minimum energy structure given in the literature and validates both, the use of the PIP-PES in the present work and the NEB approach.¹² The minimum energy structure for the PIP-PES is, however, 53.1 kcal/mol above the $N_2(^1\Sigma_g^+) + N(^4S)$ asymptote, see Table 1. For comparison, two additional minimum energy structures at the CCSD(T) and MR-CISD+Q levels of theory^{6,8} using the aug-cc-pVTZ basis sets were included in Table 1. Both confirm the results from the present RKHS-PES based on MRCI-F12/AVTZ-F12 calculation. Hence, the differences in the stabilization en-

Table 1: Minimum (MIN) and transition state (TS) geometries for the $^4A''$ electronic state of N_3 . The critical points were calculated using the Nudged Elastic Band (NEB)^{34,35} method. Distances in Å and a_0 (in brackets), valence angles in degrees and energies in kcal/mol relative to the $N_2(^1\Sigma_g^+) + N(^4S)$ asymptote. *The optimized structures for the PIP-based PES were determined using the NEB method to directly compare with the results given in the literature.¹²

		$r_e^{(N_A N_B)}$	$r_e^{(N_B N_C)}$	$\angle N_A N_B N_C$	ΔE
MIN	RKHS MRCI-F12/AVTZ-F12	1.26 Å (2.39 a_0)	1.26 Å (2.39 a_0)	118.2°	43.7
	PIP* CASPT2/mAVQZ	1.27 Å (2.40 a_0)	1.27 Å (2.40 a_0)	115.5°	53.1*
	PIP CASPT2/mAVQZ	1.27 Å	1.27 Å	115.6°	53.1 ¹²
	CCSD(T)/AVTZ	1.27 Å	1.27 Å	119.0°	44.7 ⁸
	MRCISD(Q)/AVTZ	1.27 Å	1.27 Å	118.5°	46.2 ⁶
TS	RKHS MRCI-F12/AVTZ-F12	1.18 Å (2.23 a_0)	1.51 Å (2.86 a_0)	118.5°	47.5
	PIP* CASPT2/mAVQZ	1.18 Å (2.23 a_0)	1.48 Å (2.80 a_0)	116.6°	56.5*
	PIP CASPT2/mAVQZ	1.18 Å	1.48 Å	116.7°	56.5 ¹²
	CCSD(T)/AVTZ	1.18 Å	1.50 Å	117.0°	47.1 ⁸
	MRCISD(Q)/AVTZ	1.18 Å	1.50 Å	117.2°	48.7 ⁶

ergy of triangular N_3 relative to the $N_2(^1\Sigma_g^+) + N(^4S)$ limit are mainly due to the methods and basis sets used.

To verify this, the dissociation energy of $N_2(^1\Sigma_g^+)$ was determined using the AVTZ-F12 and AVQZ-F12 basis sets for which $D_e^{AVTZ-F12} = 222.0$ kcal/mol and $D_e^{AVQZ-F12} = 222.6$ kcal/mol were obtained, compared with $D_e^{mAVQZ} = 228.7$ kcal/mol at the CASPT2/mAVQZ level¹² which differs by 6 to 7 kcal/mol from the MRCI-F12 calculations. Hence, part of the difference $\Delta E \sim 10$ kcal/mol for the N_3 minimum energy relative to $N_2(^1\Sigma_g^+) + N(^4S)$ (see Table 1) is explained by differences in the stabilization energy of N_2 when using MRCI-F12 or CASPT2 levels of theory.

For the transition state structure the findings are comparable. The geometries of the TS using the NEB method for the RKHS-PES and PIP-PES compare favourably whereas the

energy relative to the asymptote differs by 9.0 kcal/mol, see Table 1. The TS structure and energy from the literature¹² are confirmed by the NEB calculations using the PIP-PES. Again, using the smaller AVTZ basis set confirms both, the structure and energy of the TS relative to the $N_2(^1\Sigma_g^+) + N(^4S)$ limit from the RKHS-PES. Notably, the height of the barrier between MIN and TS structures is 3.8 kcal/mol for the RKHS-PES compared with 3.4 kcal/mol for the PIP-PES and 2.4 kcal/mol and 2.5 kcal/mol from the two earlier calculations using the aug-cc-pVTZ basis set.^{6,8} Notably, the two PESs considered in the present work are based on different methods (MRCI-F12 vs. CASPT2) and two different basis sets (AVTZ-F12 vs. mAVQZ). Given these differences, the rather close agreement for the geometries and relative energetics is notable. A final comparison between MRCI+Q/AVTZ (used in earlier work) and MRCI-F12/AVTZ-F12 levels was carried out for a 1d-cut with $r_{NN} = 2.3 a_0$, $\theta = 50^\circ$, and $R \in [2.4, 8.0] a_0$. The stabilization energies of N_3 towards dissociation to $N_2 + N$ are 18.3 kcal/mol and 17.7 kcal/mol, separated by barrier heights of 27.3 kcal/mol and 28.7 kcal/mol, respectively. Again, the effect of the basis set on relative energies is of the order of ~ 1 kcal/mol.

Validation of the PES

To validate the present RKHS-PES, thermal rates for the atom-exchange and dissociation reactions were determined, see Figures 2 and 3. First, it is of interest to briefly consider the convergence with respect to the number of reactive trajectories for a given state-to-state transition ($v = 21, j = 30, E = 2.0$) \rightarrow ($v' = 20, j' = 34$). With both PESs, 10^7 QCT trajectories were run and the rates were determined using 10^5 , 10^6 , and 10^7 trajectories. The ratios $N_{\text{reactive}}/N_{\text{tot}}$ for the RKHS-PES are 0.00558, 0.00550, and 0.00553 compared with 0.00163, 0.00180, and 0.00177 for the PIP-PES, respectively. Hence, convergence for state-to-state transitions is typically achieved for $\sim 10^5$ trajectories starting from a given initial condition.

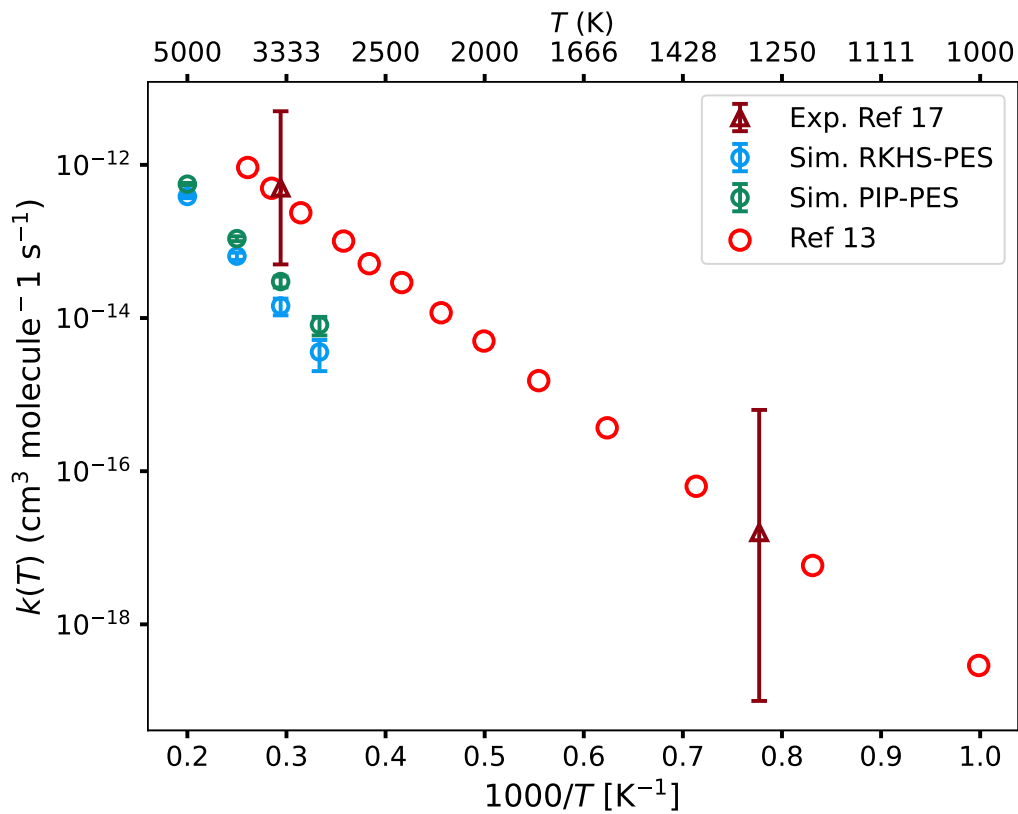


Figure 2: Thermal rates for the atom-exchange reaction from QCT simulations on the present RKHS-PES (blue) compared with those on the PIP-PES (green) computed from 10^7 trajectories for each temperature considered, experiment (red triangles)¹⁷ with error bars from a theoretical study⁸ and from transition state theory (red circles).¹³ The number/percentage of reactive trajectories from simulations using the RKHS-PES at 3000, 3400, 4000, and 5000 K range from 58 ($\sim 10^{-4}\%$) to 4192 ($\sim 4 \times 10^{-2}\%$), compared with 124 ($\sim 10^{-3}\%$) to 6342 ($\sim 6 \times 10^{-2}\%$) for the PIP-PES.

Exchange Reaction: The results for the atom exchange reaction ($N_A N_B + N_C \rightarrow N_A N_C + N_B$) from simulations at 5000, 4000, 3400, and 3000 K together with associated error bars from bootstrapping using the two reactive PESs are given in Figure 2. The electronic degeneracy factor for this reaction is $g_e = 1$. The fraction of reactive trajectories ranges from $\sim 10^{-2}\%$ to $\sim 10^{-4}\%$. All computed rates are smaller than the TST rates (red open circles). Compared with the only experiment available in this temperature range (at 3400 K), the computed $k(T)$ is within error bars from the two QCT-derived rates, but with somewhat better agreement for the PIP-PES. Since the fraction of reactive trajectories is only $\sim 10^{-4}\%$ at 3000 K, it is unfeasible to determine thermal rates directly from QCT simulations as the estimated number of trajectories required for convergence would be on the order of $> 10^9$. The overall temperature-dependence is correctly described by the present simulations although the slope of $k(T)$ appears slightly steeper than in the experiments.

Atomization Reaction: For the atomization reaction $N_2(^1\Sigma_g^+) + N(^4S) \rightarrow N(^4S) + N(^4S) + N(^4S)$, the thermal rates are reported in Figure 3. Formally, the degeneracy factor based on statistical mechanics is $g_e = 16$; however $g_e = 1$ was used in the following to not inflate rates based on symmetry considerations only. The temperature dependence of both QCT-based simulations (blue for RKHS-PES and green for PIP-PES) follows the experimentally reported rates (red).¹⁸ The computed $k^{\text{RKHS}}(T)$ from simulations using the RKHS-PES is larger by about one order of magnitude than the experiment (within error bars). Simulations using the PIP-PES yield $k^{\text{PIP}}(T)$ that follows the experimentally reported rates rather closely. Nevertheless, $k^{\text{RKHS}}(T)$ still correctly describes the reported T -dependence if scaled with a constant factor (brown symbols in Figure 3).

The PIP-PES was recently used in simulations and a NN-based model for the atomization reaction.¹⁶ For equal rotational and vibrational temperatures these results can be directly compared with those obtained in the present work, see magenta crosses and green circles

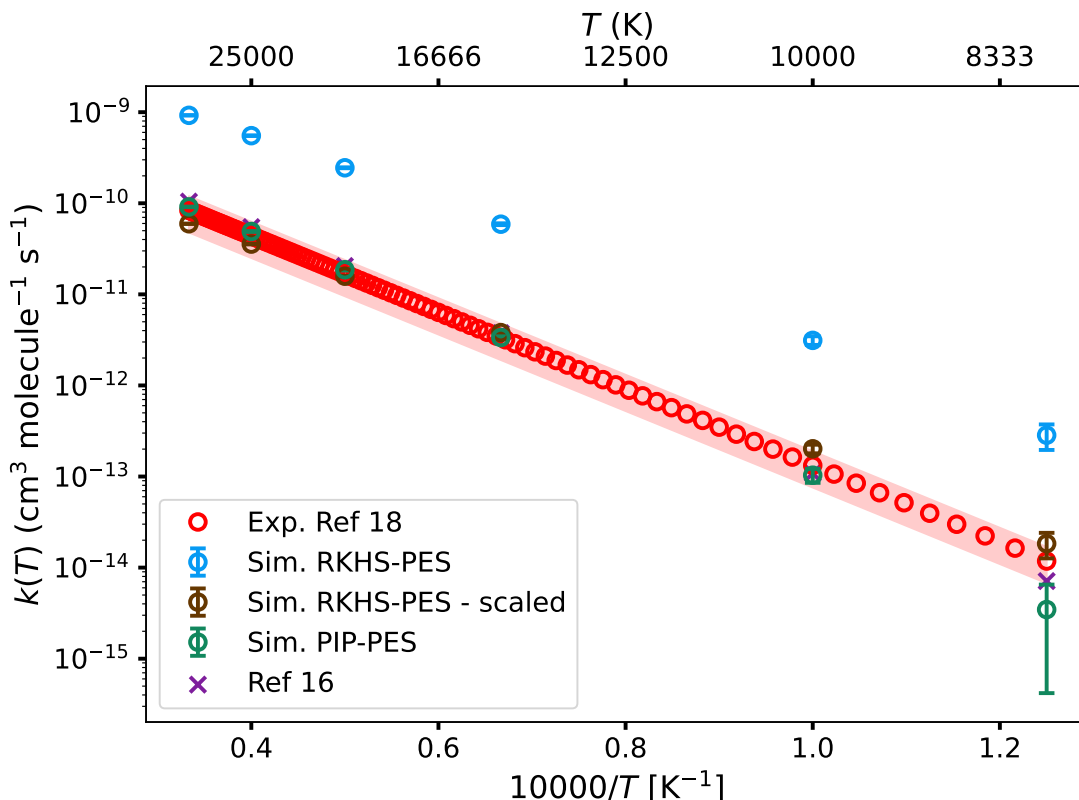


Figure 3: Thermal rates for the atomization reaction from QCT simulations on the present RKHS-PES (blue) and the PIP-PES (green) computed from 10^7 trajectories for every temperature considered. The experimental data are the red circles.¹⁸ For both PESs, statistical errors are reported from bootstrapping using 10 sub-batches with a 10^6 sample size and conducted 10 times in random order. For $T = 8000, 10000, 15000, 20000, 25000,$ and 30000 K, the number of reactive trajectories (10^7 for each T) on the RKHS-PES range from $\sim 10^{-3}$ % to ~ 8 % (435, 3899, 64713, 239998, 489896, 759432) compared with $\sim 10^{-4}$ % to ~ 2 % (17, 406, 11803, 57065, 136537, 235190) for the PIP-PES. Hence, for converged rates at 8000 K a larger number of trajectories would be required. To demonstrate the correct T -dependence of the rates from the RKHS-PES, the results are scaled (brown) to best overlap with the experimental reference. The purple crosses are from QCT calculations on the PIP-PES¹⁶ which agree closely with the present simulations (green).

in Figure 3. The close agreement is a mutual and independent validation of both QCT-simulations.

Overall, the RKHS- and PIP-based PESs yield comparable results with differences in the details. QCT simulations for the atom exchange and atomization reactions yield thermal rates $k(T)$ in good to reasonable agreement with experiments within error bars, whereas for the atomization reaction, the PIP-PES performs better but the results using the RKHS-PES also show the correct T -dependence. The possible reason for the larger $k(T)$ of the atomization reaction for the RKHS-PES is the lower barrier to reach the transition state coming from $\text{N}_2(1\Sigma_g^+) + \text{N}(4\text{S})$, see Table 1, and the lower N_2 -dissociation energy.

Final State Distributions and NN-Based Model

Next, the final state distributions for translational, vibrational and rotational degrees of freedom were determined for the atom-exchange reaction using the two PESs. As reported above, both PESs (RKHS-PES and PIP-PES) perform comparably for this reaction. The product state distributions $P(E'_{\text{trans}})$, $P(E'_{\text{int}})$, $P(v')$, and $P(j')$ from particular initial conditions $[E_{\text{trans}}, v, j]$ are analyzed and compared in the following and STD models were generated for both PESs.

It is of interest to compare final state distributions from QCT simulations using both PESs for a few representative but randomly chosen initial conditions, see Figure 4. Results for three initial conditions using the RKHS-PES as detailed in the caption of Figure 4 are shown as solid lines and compared to those for the PIP-PES (open circles). The top row in Figure 4 reports the actual final state distributions whereas the bottom row shows the difference between the distributions using the two PESs. The overall shapes for the final state distributions for the same initial state using the two different PESs are comparable for these

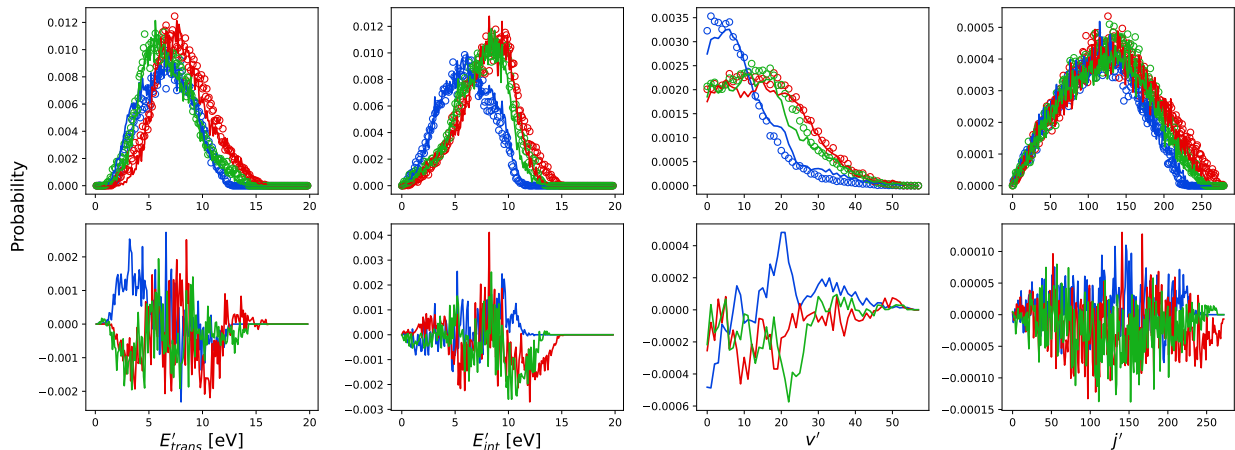


Figure 4: Product QCT distribution for the $4A''$ PES_{Truhlar} and PES_{Unibas} from 3 initial conditions: $[v = 2, j = 180, E_{\text{trans}} = 5.0 \text{ eV}]$ (blue), $[v = 6, j = 225, E_{\text{trans}} = 4.5 \text{ eV}]$ (red) and $[v = 10, j = 180, E_{\text{trans}} = 5.0 \text{ eV}]$ (green). The final E'_{trans} , E'_{int} , v' , and j' are plotted as a function of the reaction probability. The probability is computed using histogram binning. The top panels show the final state distributions of the two PES's, RKHS-PES (solid line) and PIP-PES (open circles), and the bottom panels report the difference between the distributions of the two PESs in the corresponding colors.

particular initial conditions, specifically for $P(E'_{\text{trans}})$, $P(E'_{\text{int}})$, and $P(j')$, whereas for $P(v')$ slight differences are present.

Next, a broader set of initial conditions was generated. Specifically, all 4 combinations of small and large values for initial v and j for a range of initial translational energies E_{trans} and final state distributions were determined from QCT simulations using both PESs, see Figure 5. Qualitatively, $P(E'_{\text{trans}})$, $P(E'_{\text{int}})$ and $P(v')$ from simulations using the two PESs agree with each other whereas for $P(j')$, the second maximum for large j' is absent from simulations using the PES-PIP. The high- j' distributions (green and blue in the right column of Figure 5) from simulations using the RKHS-PES mainly originate from rather high initial $v \geq 20$ and high initial $j \geq 150$ states. In Figure 5, the high j' distributions correspond to initial condition $(v = 30, j = 150)$ and $(v = 21, j = 195)$, regardless of the initial E_{trans} . Given the topographies of the two PESs it is conceivable that these differences arise due to the different angular anisotropies of the RKHS-PES and PIP-PES.

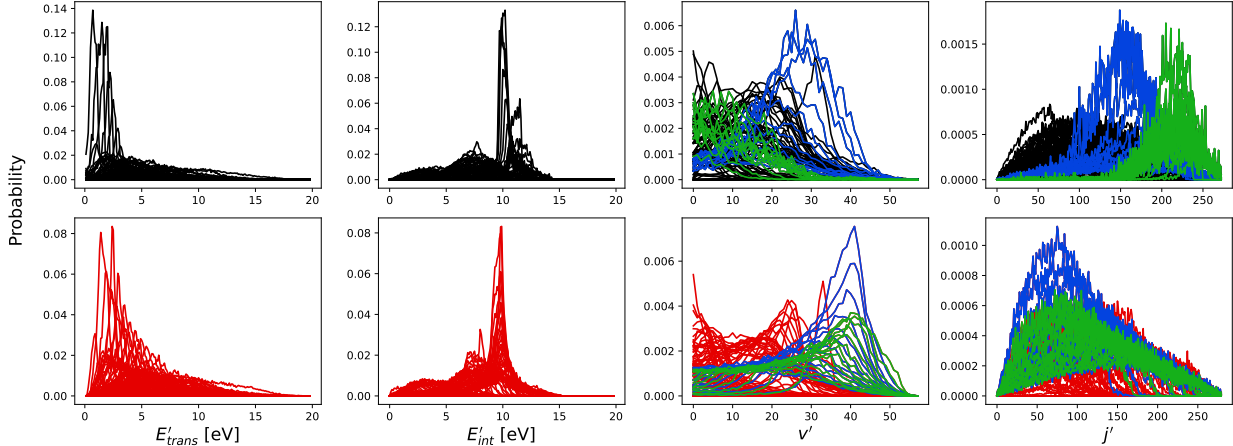


Figure 5: Product QCT distribution for the $4A''$ RKHS-PES and PIP-PES for several sets of initial conditions. The final E'_{trans} , E'_{int} , v' , and j' are plotted as a function of the reaction probability. The upper row contains final distributions for the RKHS-PES, while the bottom row contains final distributions for the PIP-PES using the same sets of initial conditions. Blue and green curves in both panels correspond to initial conditions ($v = 30, j = 150$) and ($v = 21, j = 195$), respectively, including all E_{trans} .

Finally, STD models were trained following the procedures described in the methods section for both PESs. The performance of both trainings is reported in Figures 6 and 7. For both models the performance on the test set is reported and comparisons between reference QCT simulations and trained models are given for the best, the average and the worst performing final state distributions together with the R^2 -value between the NN-model and the results from explicit QCT simulations.

For the STD model using QCT results based on the RKHS-PES, the overall R^2 on the training and test sets is 0.97 compared with 1.00 and 0.99 for the data based on QCT simulations using the PIP-PES. During training, the errors drop more rapidly for the data related to the PIP-PES compared to that from the RKHS-PES. A possible reason is that the RKHS-PES tends to give broader final state distributions, in particular for $P(j')$ and $P(v')$, than the PIP-PES out of QCT simulations for the same initial conditions, see Figure 5. This also suggests that the RKHS-PES is somewhat more anisotropic than the PIP-PES. Consequently,

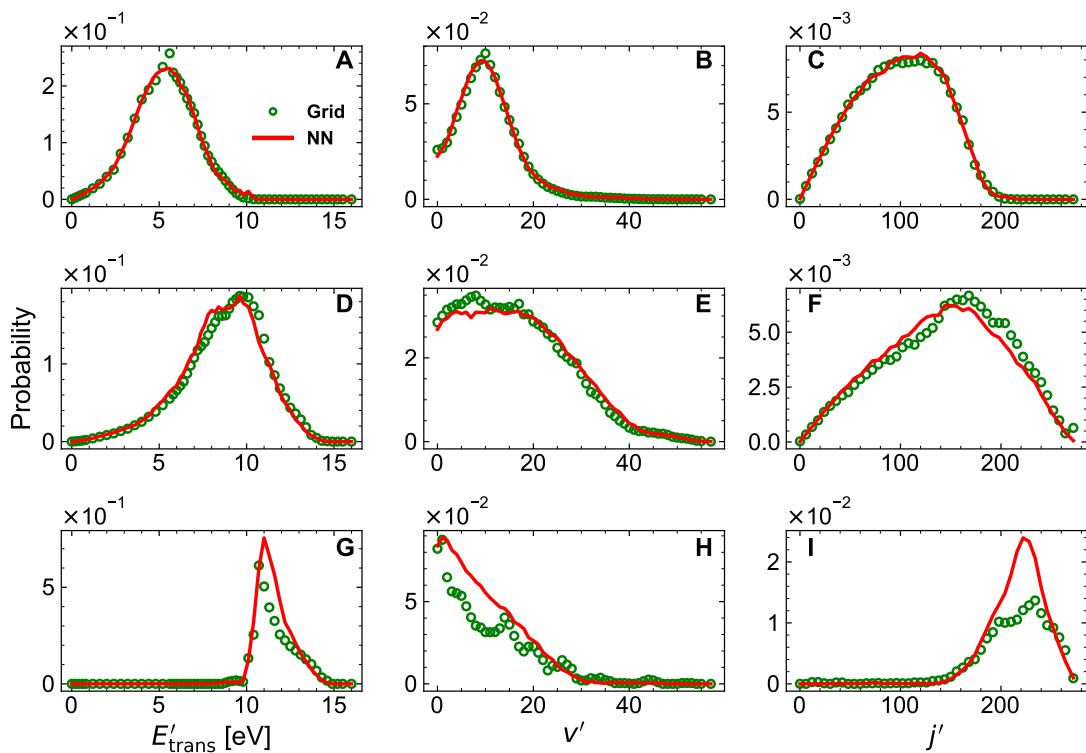


Figure 6: STD Model for final state distributions from QCT simulations using the RKHS representation for the $^4A''$ state $\text{PES}_{\text{Basel}}$. Reference amplitudes (Grid) obtained from taking moving averages of the raw QCT data in comparison to STD predictions (NN). The final E'_{trans} , v' , and j' are plotted as a function of the reaction probability. Three cases for the quality of the NN-trained models are distinguished: initial condition for which the prediction is best (A to C, highest $R^2 = 1.00$), is closest to the average R^2 (D to F, $R^2 = 0.97$), and worst (G to I, $R^2 = 0.64$). The corresponding initial conditions are $[E_{\text{trans}} = 4.5 \text{ eV}, v = 12, j = 75]$; $[E_{\text{trans}} = 7.0 \text{ eV}, v = 21, j = 150]$; $[E_{\text{trans}} = 4.0 \text{ eV}, v = 27, j = 210]$ for the best, mean and worst cases, respectively.

it requires a larger number of QCT trajectories to access all the final states for the RKHS-PES than for the PIP-PES, and training the STD-NN model to reach the same level of accuracy typically requires more data from simulations using the RKHS-PES. In this work, the simulation outputs with final $P(v') < 0.02$ were discarded from the training set, which results in 1900 samples (out of 2360 samples in total) used as the training set for the RKHS-PES, while the training set of PIP-PES contains 2000 samples (out of 2314 samples in total).

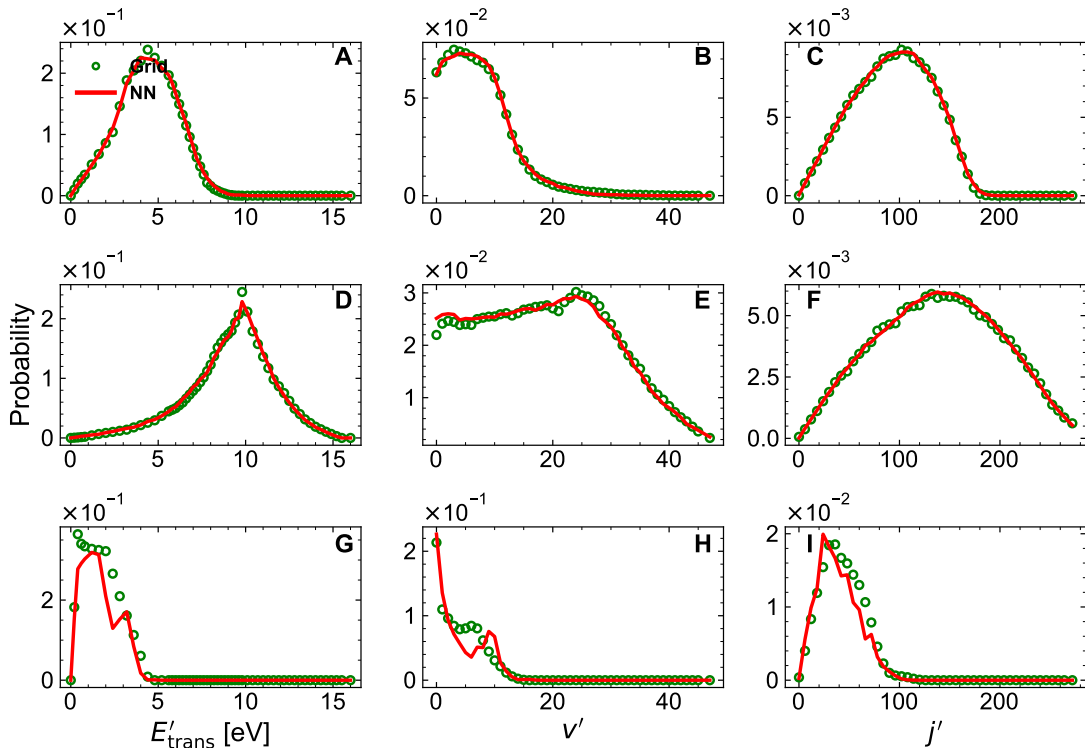


Figure 7: STD Model for final state distributions from QCT simulations using the PIP-PES for the $4A''$ state. Reference amplitudes (Grid) obtained from taking moving averages of the raw QCT data in comparison to STD predictions (NN). The final E'_{trans} , v' , and j' are plotted as a function of the reaction probability. Three cases for the quality of the NN-trained models are distinguished: initial condition for which the prediction is best (A to C, highest $R^2 = 1.00$), is closest to the average R^2 (D to F, $R^2 = 0.99$), and worst (G to I, $R^2 = 0.92$). The corresponding initial conditions are $[E_{\text{trans}} = 3.5 \text{ eV}, v = 4, j = 150]$; $[E_{\text{trans}} = 6.0 \text{ eV}, v = 12, j = 225]$; $[E_{\text{trans}} = 2.5 \text{ eV}, v = 10, j = 0]$ for the best, mean and worst cases, respectively.

Discussion and Conclusions

This work investigates thermal rates and final state distributions for the $\text{N}(^4\text{S}) + \text{N}_2(^1\Sigma_g^+)$ collision system using a new, global RKHS-represented PES of high quality. Extensive reference calculations were carried out at the MRCI-F12/AVTZ-F12 level of theory to be consistent with previous work on thermal rates and final state distributions for the [NNO], [OON], and [OOC] collision systems.^{23–26} This will allow consistent modeling and incorporation of the relevant microscopic information - such as state-to-state or thermal rates - in reaction networks encompassing all these species.² The MRCI-F12/AVTZ-F12 method was chosen here due to its improved convergence properties over MRCI+Q/AVTZ but differences in the relative energetics between the two methods are found to be small, typically of the order of a few percent.

The N_3 -PES was validated for the atom exchange and atomization reactions using an extensive distribution of initial states. For the atom exchange reaction, the thermal rates $k(T)$ are in good agreement with experiment within error bars, whereas for the atomization reaction, the computed rates are larger than those from experiment by about one order of magnitude. However, the temperature-dependence is correctly captured. Atomization rates using the PIP-PES were found to agree with recent simulations and with experiment, validating the overall QCT-simulation strategy used here.

The overestimation of the rate for atomization using the RKHS-PES can be traced back to differences in the MRCI-F12 and CASPT2 methods and the basis sets used. First, the N_2 molecule is less stable using the MRCI-based RKHS-represented PES than with the CASPT2-based PIP representation. To obtain the relevant diatomic potentials $V(r)$, the third nitrogen atom was placed $500 a_0$ away from the center of mass of N_2 and the N_2 bond length r scanned. Well depths and dissociation energies for N_2 are $D_e^{\text{RKHS}} = 226.0$ kcal/mol, $D_0^{\text{RKHS}} = 222.9$ kcal/mol, compared with $D_e^{\text{PIP}} = 228.4$ kcal/mol, $D_0^{\text{PIP}} = 225.1$ kcal/mol.

Both D_0 -values compare favourably with recent experiments that reported $D_0^{\text{exp}} = 225$ kcal/mol,³⁶ but the CASPT2-PIP PES is clearly superior for N_2 -dissociation by construction because the electronic structure calculations were carried out with this purpose in mind, see Methods Section. The bound states for N_2 were determined using the LEVEL-program.³⁷ A second difference between the two PESs is the height of the barrier to form bent N_3 which is lower by 9 kcal/mol for the RKHS-PIP PES (see Table 1 and Figure 1B). These two effects contribute to finding a higher thermal rate for the atomization reaction using the RKHS-PES. Comparable differences of 1 to 3 kcal/mol between MRCISD(Q) and CASPT2 energies using the AVTZ basis set for triangular N_3 and the TS separating from the $\text{N}(^4\text{S}) + \text{N}_2(^1\Sigma_g^+)$ asymptote were already reported in earlier work.⁶ Possibilities to further improve the RKHS-PES (e.g. adjust the barrier to form bent quartet- N_3) include PES-morphing using information from the CASPT2 PES as has recently been done for He-H_2^+ ,³⁸ or to use transfer learning techniques.³⁹

Finally, it is of interest to consider the probability for stabilizing bent- N_3 . First, none of the simulations indicated that c- N_3 can be stabilized for the entire 75 ps for which the QCT simulations were run. In all cases either atom exchange, atomization or elastic/inelastic scattering occurred. However, it is possible that c- N_3 forms transiently and a number of atom-exchange trajectories were analyzed to this end, see Figure 8.

In summary, QCT simulations using the RKHS-based PES for the $\text{N}(^4\text{S}) + \text{N}_2(^1\Sigma_g^+)$ collision system yielded thermal rates for the atom exchange reaction in favourable agreement with experiments. The temperature-dependence for the atomization reaction is consistent with experiments but overestimates absolute values by one order of magnitude. However, it is straightforward to account for this in subsequent reaction network simulations. For a comprehensive description of the state-dependent rates, STD models for both PESs were determined from an NN-based approach. The performance of both STD models is on par

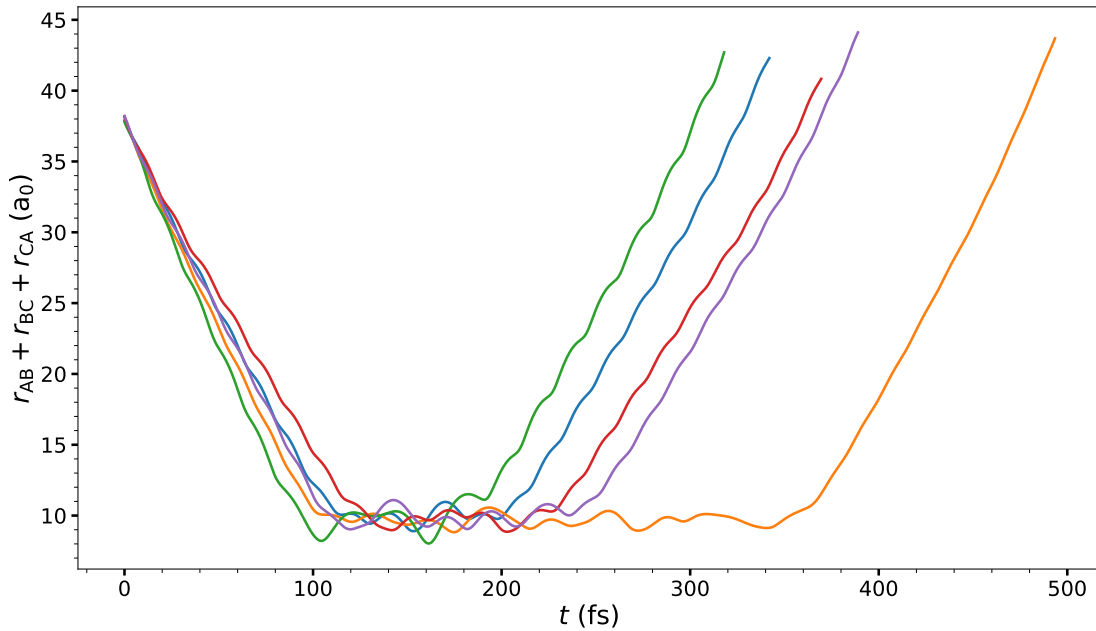


Figure 8: Sum $\rho(t) = r_{AB}(t) + r_{AC}(t) + r_{BC}(t)$ of atom-atom separations as a function of simulation time. N_3 in its local minimum energy structure for $\rho(t) \simeq 9 a_0$, see Table 1. Typical lifetimes are on the 200 fs time scale. Initial conditions are $(E_{\text{trans}} = 3.5 \text{ eV}, v = 1, j = 2)$ (blue), $(E_{\text{trans}} = 4.0 \text{ eV}, v = 1, j = 2)$ (orange), $(E_{\text{trans}} = 4.5 \text{ eV}, v = 1, j = 2)$ (green), $(E_{\text{trans}} = 3.0 \text{ eV}, v = 2, j = 2)$ (red), $(E_{\text{trans}} = 3.5 \text{ eV}, v = 2, j = 2)$ (lila).

with previous systems.^{20–22,40,41} The combination of high-level electronic structure calculations, machine-learning-based representation of the corresponding PES, QCT dynamics simulations, and NN-based modeling of the entire initial and final state space provides a meaningful way to describe the reaction dynamics of atom + diatom reactions.

Data Availability

The RKHS-PES, the two STD models, and one video for the atom exchange reaction are available at <https://github.com/MMunibas/N3>.

Acknowledgment

We thank the United State Department of the Air Force (AFOSR), the Swiss National Science Foundation (grants 200021_117810, 200021_215088, and the NCCR MUST) (to MM), and the University of Basel for supporting this work. Valuable discussions with Proff. D. Koner, G. Schatz and H. Guo are acknowledged.

References

- (1) Park, C. *Nonequilibrium Hypersonic Aerothermodynamics*; Wiley-Interscience: New York, 1990.
- (2) Boyd, I. D.; Schwartzentruber, T. E. *Nonequilibrium Gas Dynamics and Molecular Simulation*; Cambridge University Press, 2017; Vol. 42.
- (3) Atreya, S. K.; Donahue, T. M.; Kuhn, W. R. Evolution of a nitrogen atmosphere on Titan. *Science* **1978**, *201*, 611–613.

- (4) Vuitton, V.; Yelle, R.; Anicich, V. The nitrogen chemistry of Titan's upper atmosphere revealed. *Astrophys. J.* **2006**, *647*, L175.
- (5) Wu, Y.-J.; Chen, H.-F.; Chuang, S.-J.; Huang, T.-P. Far Ultraviolet Absorption Spectra of N_3 and N_2^+ Generated by Electrons Impacting Gaseous N_2 . *Astrophys. J.* **2013**, *779*, 40.
- (6) Zhang, P.; Morokuma, K.; Wodtke, A. M. High-level ab initio studies of unimolecular dissociation of the ground-state N_3 radical. *J. Chem. Phys.* **2005**, *122*.
- (7) Lagana, A.; Garcia, E.; Ciccarelli, L. Deactivation of vibrationally excited nitrogen molecules by collision with nitrogen atoms. *J. Phys. Chem.* **1987**, *91*, 312–314.
- (8) Wang, D.; Stallcop, J. R.; Huo, W. M.; Dateo, C. E.; Schwenke, D. W.; Partridge, H. Quantal study of the exchange reaction for $\text{N} + \text{N}_2$ using an ab initio potential energy surface. *J. Chem. Phys.* **2003**, *118*, 2186–2189.
- (9) Garcia, E.; Saracibar, A.; Gómez-Carrasco, S.; Laganà, A. Modeling the global potential energy surface of the $\text{N} + \text{N}_2$ reaction from ab initio data. *Phys. Chem. Chem. Phys.* **2008**, *10*, 2552–2558.
- (10) Mankodi, T. K.; Bhandarkar, U. V.; Puranik, B. P. Dissociation cross sections for $\text{N}_2 + \text{N} \rightarrow 3\text{N}$ and $\text{O}_2 + \text{O} \rightarrow 3\text{O}$ using the QCT method. *J. Chem. Phys.* **2017**, *146*.
- (11) Paukku, Y.; Yang, K. R.; Varga, Z.; Truhlar, D. G. Global ab initio ground-state potential energy surface of N_4 . *J. Chem. Phys.* **2013**, *139*.
- (12) Varga, Z.; Truhlar, D. G. Potential energy surface for high-energy $\text{N} + \text{N}_2$ collisions. *Phys. Chem. Chem. Phys.* **2021**, *23*, 26273–26284.
- (13) Lago, N. F.; Laganà, A.; Gargano, R.; Barreto, P. On the semiclassical initial value calculation of thermal rate coefficients for the $\text{N} + \text{N}_2$ reaction. *J. Chem. Phys.* **2006**, *125*.

- (14) Esposito, F.; Capitelli, M. QCT calculations for the process $N_2(v) + N \rightarrow N_2(v') + N$ in the whole vibrational range. *Chem. Phys. Lett.* **2006**, *418*, 581–585.
- (15) Esposito, F.; Capitelli, M. Quasiclassical molecular dynamic calculations of vibrationally and rotationally state selected dissociation cross-sections: $N + N_2(v, j) \rightarrow 3N$. *Chem. Phys. Lett.* **1999**, *302*, 49–54.
- (16) Gu, K.-M.; Zhang, H.; Cheng, X.-L. Exhaustive state-specific dissociation study of the $N_2(^1\Sigma_g^+) + N(^4S)$ system using QCT combined with a neural network method. *J. Chem. Phys.* **2023**, *158*.
- (17) Lyon, R. K. Search for the N–N₂ Exchange Reaction. *Can. J. Chem.* **1972**, *50*, 1437–1440.
- (18) Appleton, J. P.; Steinberg, M.; Liquornik, D. J. Shock-Tube Study of Nitrogen Dissociation using Vacuum-Ultraviolet Light Absorption. *J. Chem. Phys.* **1968**, *48*, 599–608.
- (19) Bar-Nun, A.; Lifshitz, A. Kinetics of the Homogeneous Exchange Reaction: $^{14-14}N_2 + ^{15-15}N_2 \leftrightarrow 2^{14-15}N_2$. Single-Pulse Shock-Tube Studies. *J. Chem. Phys.* **1967**, *47*, 2878–2888.
- (20) Koner, D.; Unke, O. T.; Boe, K.; Bemish, R. J.; Meuwly, M. Exhaustive state-to-state cross sections for reactive molecular collisions from importance sampling simulation and a neural network representation. *J. Chem. Phys.* **2019**, *150*, 211101.
- (21) Arnold, J.; San Vicente Veliz, J. C.; Koner, D.; Singh, N.; Bemish, R. J.; Meuwly, M. Machine learning product state distributions from initial reactant states for a reactive atom-diatom collision system. *J. Chem. Phys.* **2022**, *156*, 034301.
- (22) San Vicente Veliz, J. C.; Arnold, J.; Bemish, R. J.; Meuwly, M. Combining Machine Learning and Spectroscopy to Model Reactive Atom + Diatom Collisions. *J. Phys. Chem. A* **2022**, *126*, 7971–7980.

- (23) Veliz, J. C. S. V.; Koner, D.; Schwilk, M.; Bemish, R. J.; Meuwly, M. The $C(^3P) + O_2(^3\Sigma_g) \leftrightarrow CO_2 \leftrightarrow CO(^1\Sigma^+) + O(^1D)/O(^3P)$ Reaction: Thermal and Vibrational Relaxation Rates from 15 K to 20000 K. *Phys. Chem. Chem. Phys.* **2021**, *23*, 11251–11263.
- (24) San Vicente Veliz, J. C.; Koner, D.; Schwilk, M.; Bemish, R. J.; Meuwly, M. The $N(^4S) + O_2(X^3\Sigma) \longleftrightarrow O(^3P) + NO(X^2\Pi)$ Reaction: Thermal and Vibrational Relaxation Rates for the $^2A'$, $^4A'$ and $^2A''$ States. *Phys. Chem. Chem. Phys.* **2020**, *22*, 3927–3939.
- (25) Koner, D.; San Vicente Veliz, J. C.; ; Bemish, R. J.; Meuwly, M. Accurate Reproducing Kernel-based Potential Energy Surfaces for the Triplet Ground States of N_2O and Dynamics for the $N+NO \leftrightarrow O+N_2$ Reaction. *Phys. Chem. Chem. Phys.* **2020**, *22*, 18488–18498.
- (26) Koner, D.; Bemish, R. J.; Meuwly, M. The $C(^3P) + NO(X^2\Pi) \rightarrow O(^3P) + CN(X^2\Sigma^+)$, $N(^2D)/N(^4S) + CO(X^1\Sigma^+)$ reaction: Rates, branching ratios, and final states from 15 K to 20000 K. *J. Chem. Phys.* **2018**, *149*, 094305.
- (27) Werner, H.-J. et al. MOLPRO, version 2020, a package of ab initio programs. 2020.
- (28) Bittererová, M.; Östmark, H.; Brinck, T. A theoretical study of the azide (N_3) doublet states. A new route to tetraazatetrahedrane (N_4): $N+N_3 \rightarrow N_4$. *J. Chem. Phys.* **2002**, *116*, 9740–9748.
- (29) Shiozaki, T.; Knizia, G.; Werner, H.-J. Explicitly correlated multireference configuration interaction: MRCI-F12. *J. Chem. Phys.* **2011**, *134*, 034113.
- (30) LeCun, Y. A.; Bottou, L.; Orr, G. B.; Müller, K.-R. *Neural networks: Tricks of the trade*; Springer, 2012; pp 9–48.
- (31) Glorot, X.; Bengio, Y. Understanding the difficulty of training deep feedforward neural

- networks. Proceedings of the 13th International Conference on Artificial Intelligence and Statistics. 2010; pp 249–256.
- (32) Kingma, D.; Ba, J. Adam: A method for stochastic optimization. *arXiv preprint arXiv:1412.6980* **2014**,
- (33) Abadi, M.; Barham, P.; Chen, J.; Chen, Z.; Davis, A.; Dean, J.; Devin, M.; Ghemawat, S.; Irving, G.; Isard, M., et al. Tensorflow: A system for large-scale machine learning. 12th USENIX symposium on operating systems Design and Implementation (OSDI 16). 2016; pp 265–283.
- (34) Henkelman, G.; Uberuaga, B.; Jonsson, H. A climbing image nudged elastic band method for finding saddle points and minimum energy paths. *J. Chem. Phys.* **2000**, *113*, 9901–9904.
- (35) Kolsbjerg, E. L.; Groves, M. N.; Hammer, B. An automated nudged elastic band method. *J. Chem. Phys.* **2016**, *145*, 094107.
- (36) Wang, P.; Gong, S.; Li, Y.; Mo, Y. Bond dissociation energy of N₂ measured by state-to-state resolved threshold fragment yield spectra. *J. Chem. Phys.* **2024**, *160*, 014304.
- (37) Le Roy, R. J. LEVEL 6.1. **1996**, *CP-555R*.
- (38) Horn, K. P.; Vazquez-Salazar, L. I.; Koch, C. P.; Meuwly, M. Improving potential energy surfaces using measured Feshbach resonance states. *Sci. Adv.* **2024**, *10*, eadi6462.
- (39) Käser, S.; Meuwly, M. Transfer-learned potential energy surfaces: Toward microsecond-scale molecular dynamics simulations in the gas phase at CCSD(T) quality. *J. Chem. Phys.* **2023**, *158*.
- (40) Arnold, J.; Koner, D.; Käser, S.; Singh, N.; Bemish, R. J.; Meuwly, M. Machine Learning for Observables: Reactant to Product State Distributions for Atom–Diatom Collisions. *J. Phys. Chem. A* **2020**, *124*, 7177–7190.

- (41) Arnold, J.; San Vicente Veliz, J. C.; Koner, D.; Singh, N.; Bemish, R. J.; Meuwly, M. Machine Learning Product State Distributions from Initial Reactant States for a Reactive Atom-Diatom Collision System. *J. Chem. Phys.* **2021**, *156*, 034301.

The Potential Energy Surfaces

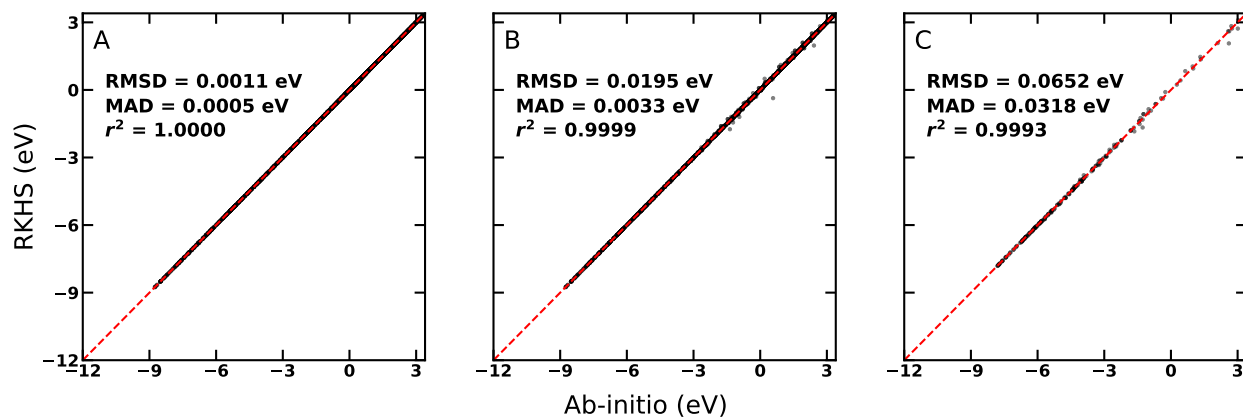


Figure S1: Correlation between the RKHS energies for on-grid data on the single channel PES (panel A), for on-grid data on the 3D channel PES (panel B), and for the off-grid validation data in comparison to the *ab initio* energies (panel C), respectively. The statistical measures (root mean squared difference - RMSD, mean absolute deviation - MAD, and r^2) for each case are given in the panels. The RMSEs/MADs are 0.03/0.01 kcal/mol, 0.45/0.08 kcal/mol, and 1.50/0.73 kcal/mol from left to right.

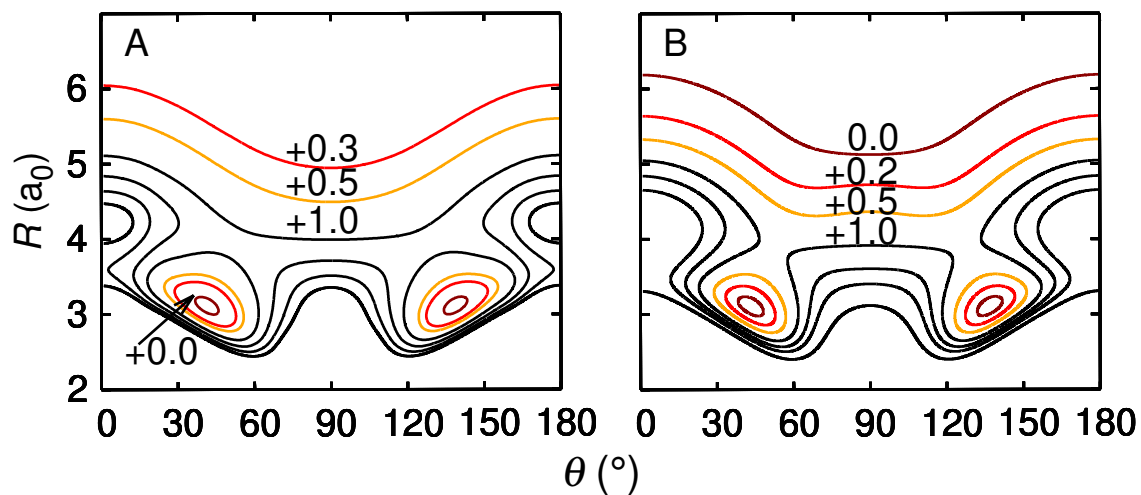


Figure S2: 2D contour representations of $V(R, \theta)$ at $r_{\text{NN}} = 2.5 a_0$ for the RKHS-PES (panel A) and for the PIP-PES (panel B).¹² Isocontours are labelled by energy difference in eV with respect to the global minimum of the specific cut of the PES. Contours at higher energies than the +1.0 eV line are at +1.5, +2.0, and +2.5 eV, respectively.

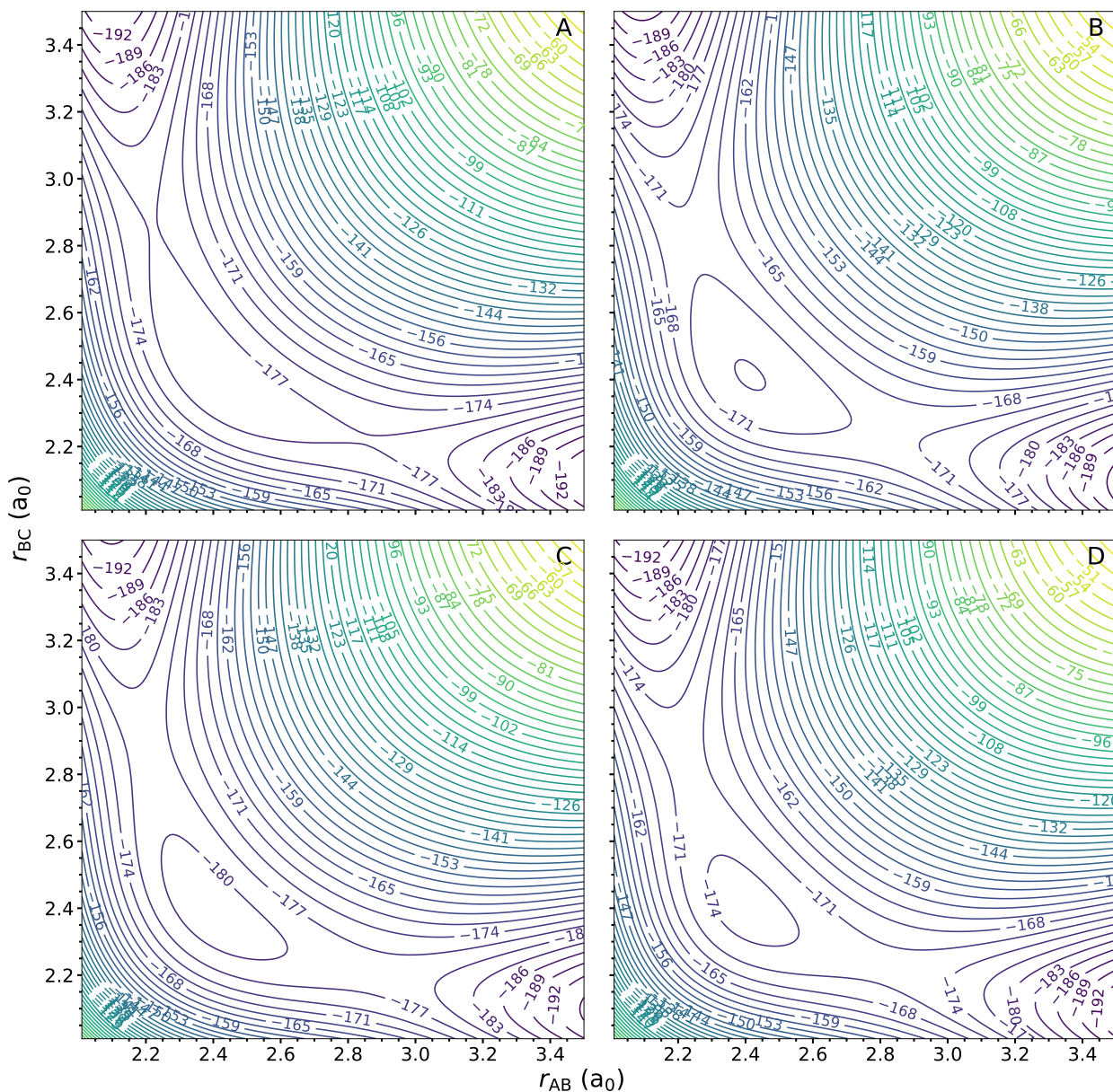


Figure S3: Comparison between the RKHS-PES (left column) and the PIP-PES (right column) for $N_A-N_B-N_C$ bond angles 110° (top panels) and 116° (bottom panels). Panels A to D show isocontours of the RKHS-PES at bond angle 110° ; PIP-PES at bond angle 110° ; RKHS-PES at bond angle 116° ; PIP-PES at bond angle 116° . r_{AB} and r_{BC} are separations N_A-N_B and N_B-N_C , respectively. Energies are in kcal/mol.